ELSEVIER

Materials Science and Engineering A311 (2001) 83–99

MATERIALS SCIENCE & ENGINEERING A

www.elsevier.com/locate/msea

Combustion synthesis/densification of an Al_2O_3–TiB_2 composite

M.A. Meyers [a], E.A. Olevsky [b,*], J. Ma [b], M. Jamet [a]

[a] *Department of Mechanical and Aerospace Engineering, University of California, San Diego, La Jolla, CA 92093, USA*
[b] *Department of Mechanical Engineering, College of Engineering San Diego State University, 5500 Campanile Drive San Diego CA 92182–1323, USA*

Received 28 July 2000; received in revised form 18 December 2000; accepted 21 December 2000

Abstract

The self-propagating gasless combustion reaction $3TiO_2 + 3B_2O_3 + 10Al \rightarrow 5Al_2O_2 + 3TiB_2$ was used to produce an Al_2O_3–TiB_2 composite, which was densified by uniaxial loading immediately following completion of reaction. The densification was enabled by the high temperatures produced by the combustion reaction (≈ 2000°C) which rendered the reaction product ($\approx 70\%$ porosity) plastic. The microstructure was characterized by columnar TiB_2 grains with a diameter of 1–2 μm and length of 5–10 μm embedded in equiaxed $A1_2O_3$ (grain size $\approx 50\mu m$); the TiB_2 phase tended to agglomerate in clusters. A few of the TiB_2 grains exhibited dislocations, while the $A1_2O_3$ was annealed. This indicates that recovery processes took place after the plastic deformation involved in densification. Several constitutive models (corresponding both to rigid-plastic and power-law creep material behavior) were used to describe the mechanical response of the porous and ductile ceramic product and compared to the experimental results, with satisfactory agreement for power-law creep models. These constitutive models have a temperature-dependent term that incorporates the effect of specimen cooling, that occurs concurrently with densification; thus, it was possible to obtain a flow stress dependence of temperature which is in reasonable agreement with values interpolated from literature experimental results.

Keywords: Combustion synthesis; Densification; Constitutive models

1. Introduction

Combustion synthesis, also known as SHS, was pioneered by Merzhanov and co-workers [1–4] and is being intensely studied in the US [5–11] and Japan [12–16]. A self-propagating gasless (virtually) combustion wave is initiated at one or more regions by an external local heat source or by heating the sample to a sufficient temperature. The fundamental aspects of the process are described by Munir and Anselmi-Tamburini [17] and Yi and Moore [18], among others. The production of dense ceramic, intermetallic, or composite compacts can be accomplished in two basic manners: (a) by comminuting the SHS product, and repressing it using high temperatures and pressures; (b) by taking advantage of the high temperature generated in the (porous) combustion product and applying the pressure while it is still hot and ductile. Niiler and co-workers [19,20] and Thadhani and co-workers [21] have applied dynamic pressures by means of explosively accelerated systems, whereas Meyers and co-workers [22,23] have used a high-speed forging machine. Very little is known about the mechanical response of the porous combustion synthesis products. The research program whose results are herein described had two principal objectives:

(a) to determine whether the reaction

$$3TiO_2 + 3B_2O_3 + 10Al \rightarrow 5Al_2O_3 + 3TiB_2 \quad (1)$$

could be used to produce dense compacts by sequential SHS-densification. This reaction uses raw materials that are technologically much more attractive than the Ti + 2B [24] and Ti + C [25] reactions due to the significant cost savings. The cost of B_2O_3 is only one small fraction ($< 1/100$) of that of boron, and TiO_2 is considerably less expensive ($< 1/10$) than titanium. Logan and coworkers [26,27] developed this reaction and applied it, in a two-stage process (SHS + grinding + hot pressing), to the production of the TiB_2–Al_2O_3 composite.

* Corresponding author. Tel.: +1-619-5946329; fax: +1-619-5943599.
E-mail address: olevsky@kahuna.sdsu.edu (E.A. Olevsky).

0921-5093/01/$ - see front matter
PII: S0921-5093(01)00930-3

(b) to develop a methodology to experimentally measure the compressive strength of combustion synthesis products and to couple it with a model in order to obtain a predictive capability of the densification processes. This predictive capability is important in the design of densification equipment.

2. Experimental methods

2.1. Starting materials and pre-combustion densification

The raw reactant materials were obtained in powder form with TiO_2 and B_2O_3 powders already mixed in the right proportions. Titanium dioxide powder (purity 99.1%) was of pigment grade with a submicron average particle size (0.3 μm) while the boron oxide particle size was less than 40 μm with a purity of 98.8%. Fig. 1(a) shows the $TiO_2 + B_2O_3$ powder mixture morphology. Both these powders were originally supplied by Fisher Scientific (Springfield, NJ). The submicron TiO_2 particles are clearly seen agglomerated on less differentiable larger B_2O_3 particles. The 99.7% pure elemental aluminum powder (Atomized Powder Grade 123) supplied by ALCOA (Aluminum Company of America, Rockdale, TX) displays a heterogeneous distribution of particles with an average diameter less than 20 μm (APD: 15–19 μm) as illustrated in Fig. 1(b). The impurity levels of the three powders were below 0.2%.

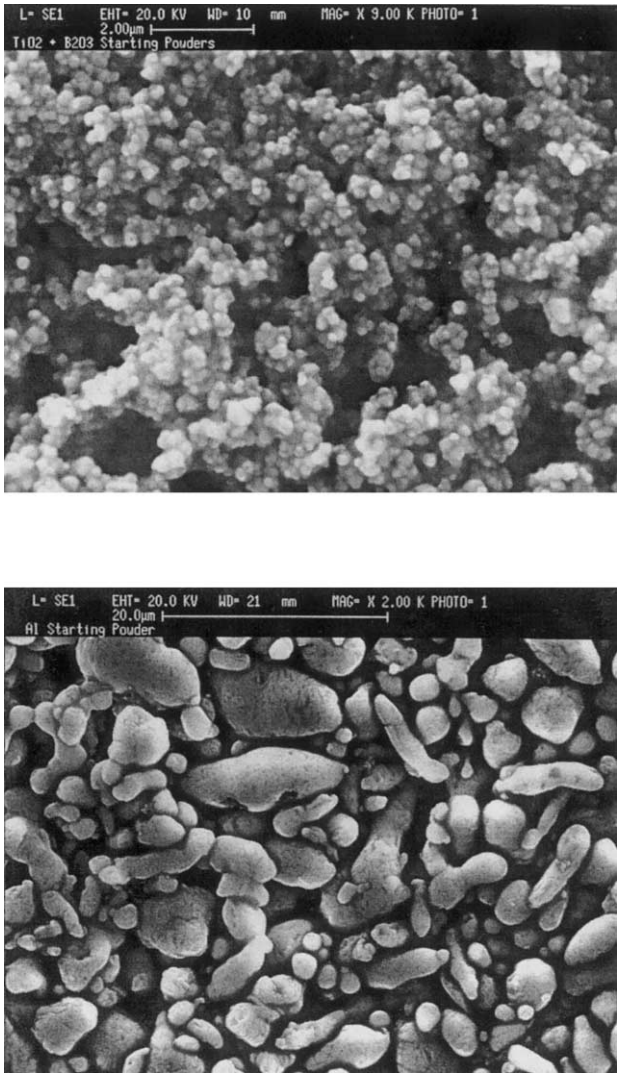

Fig. 1. Scanning electron micrographs of (a) the as-received titanium dioxide and boron oxide powder mixture particle morphology, and (b) the as-received aluminum powder.

2.2. Green compacts

The TiO_2, B_2O_3, and Al powders were dry mixed in the ratio of 33.3 wt.% TiO_2, 29.1 wt.% B_2O_3 and 37.6 wt.% Al which corresponds to the stoichiometric reaction (1). The mixing was done under argon atmosphere in a glove box. Subsequent milling was accomplished in a PVC jar with alumina cylindrical pellets (2.75% SiO_2) as grinding medium for several hours (≈ 4 h) in order to obtain a homogeneous mixture. The mixed powders were then dried in a vacuum furnace for several hours at low temperature (≈ 90°C) in order to minimize the amount of water in the reactants. It has been noticed by Logan et al. [26] that extremely violent reactions occurred when the raw materials were allowed to acquire water. Care was then taken to use dry powders. The formation of high temperature gases can produce internal pressures, which result in the explosion of the compact during combustion synthesis. After mixing and drying, the powder mixture was uniaxially cold pressed in stainless steel dies to form cylindrical 'green compacts'. A thin sheet of graphite-foil 'graphoil' obtained from Ucar Carbon (Smithtown, NY) was put inside the dies to act as a lubricant during pressing; this ensured a more homogeneous densification. For static compaction, the diameter of the unreacted pressed compacts is 31.75 mm with heights of either 19 or 38 mm. A 110 MPa pressure was used to obtain a 'green' density of 70% of the theoretical density (46% theoretical of the products) of the reactants.

The relatively high starting density (70%) was chosen as a trade-off between the great volume change during the conversion of the reactants ($\Delta V = -28\%$) and the satisfactory ignitability of the reaction by loose powder in the compact with such starting density.

2.3. Specimen containment assemblies and post-combustion densification

Containment assemblies were used to provide a strong confinement for the lateral flow induced by uniaxial hot forging or repressing (uniaxial strain compression). Their role is also to thermally insulate the reacted sample in order to reduce heat losses prior and

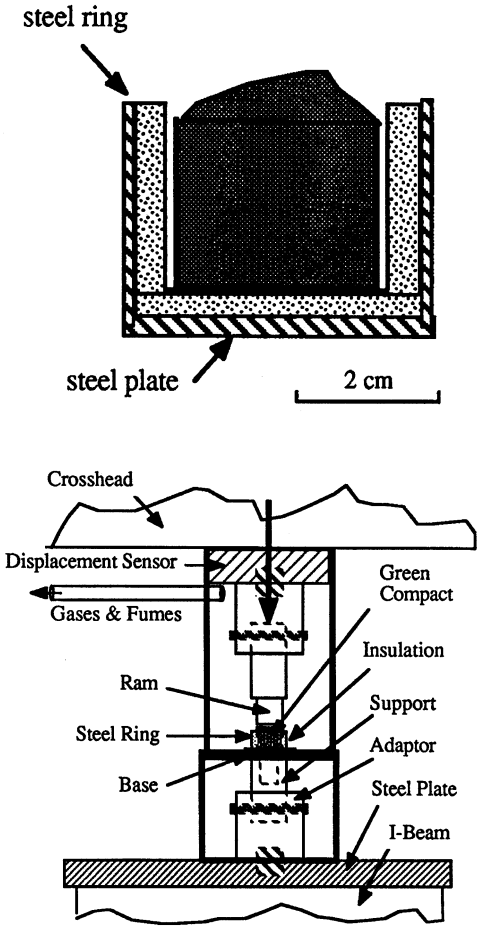

Fig. 2. Schematic representations of (a) the containment assembly for post-combustion densification, and (b) the working area on the screw-driven machine.

during compaction. Fig. 2(a) shows the assembly. The container is made of an outer stainless steel containment ring on which refractory tiles are pasted, cut from an alumina–silica sheet using alumina cement as glue. The pasted bottom was also made of the same white refractory material. Between the insulation layer and the reacting sample, a sheet of graphite foil is introduced along with a sheet of zirconia between graphite and alumina. The steel ring had an inside diameter of 44.5 mm and walls 1.58 mm thick. The bottom layer of refractory sheet was placed on top of a bottom steel plate of the same thickness as that of the steel ring.

The hot pressing of the reacted material was conducted in an electromechanical, screw driven, universal testing machine. During the static consolidation experiments, it was possible to record load–displacement curves, which are essential for the determination of the yield strength of hot porous materials (TiB_2–Al_2O_3 composite in that case). For the purpose of this investigation, the machine was modified by the addition of an I-beam on the lower part as can be seen in Fig. 2(b). This provided a base for the hot pressing experiments while the testing area was adapted to receive the reaction synthesis samples. A plexiglass cylinder was affixed on the crosshead with a hose for the evacuation of gases and fumes evolved during the reaction.

2.4. Reaction and compaction procedures

The procedure used in igniting and densifying the powder is given below. The green compact with its graphite foil sheet is introduced into the specimen containment assembly (see Fig. 2a) and loose reactant powder is put on top of the compact for ignition. The entire setup is then installed over a piece of refractory sheet on the lower fixture, centered and aligned with the ram. An electric match has to be embedded in the loose powder ready to be set off with a 12 V battery. The exhaust system is turned on. The loose powder is ignited by the electric match and the reaction propagates to and through the compact. Once the combustion wave reaches the bottom of the compact, the still red hot porous material is densified by the vertical motion of a ram (Fig. 2b). The disks generally displayed radial cracks due to thermal stresses developed during cooling.

2.5. Characterization and mechanical testing

After cooling and removal of the alumina shell, the cracked disks of dense TiB_2–Al_2O_3 were sectioned and the central region samples were separated for density and microhardness measurements and both optical and electron microscopy (SEM, TEM).

The density of the composite was determined using Archimedes' principle and compared to the theoretical density of TiB_2–Al_2O_3 calculated to be 4.12 g/cm^3 (rule of mixtures). Vickers microhardness measurements were done on polished surfaces under a 300 g test load. Specimens were prepared for optical and scanning electron microscopy using diamond-based grinding and polishing techniques. Some of them were etched in a solution consisting of 4 parts HF, 1 part HNO_3 and 3 parts water to reveal the TiB_2 phase microstructure. Polished samples required a back-scattered electron imaging technique to emphasize the phase contrast (TiB_2 and $A1_2O_3$). X-ray diffraction (XRD) analysis was performed on as-mixed and as-reacted powder samples. Specimens for transmission electron microscopy were prepared by slicing bulk samples on a low speed diamond saw into wafers and subsequently ultrasonically cutting 3-mm-diameter disks. These disks were then ground to 100 μm, mechanically dimpled to 40 μm, and finally ion-milled to electron transparency. Conventional TEM imaging and diffraction were conducted at a 300 kV accelerating potential.

3. Results and discussion

3.1. Uncompacted material

The uncompacted reacted specimens displayed a very porous microstructure independently of the mass and dimensions of the starting green compacts. During reaction, a great amount of gases and fumes was expelled, consistently with the results of Kecskes and Niiler [20]. The extent of such an outgassing appeared to be much more important than what usually occurs during synthesis of both titanium carbide and titanium diboride, even though the reactant powders were baked for several hours prior to cold pressing and subsequent reaction. The presence of impurities in the raw reactant materials may explain the large quantity of gases expelled. Baking of the reactant powders was found to eliminate a violent reaction due to the presence of water reported by Logan and Walton [26]. In our experiments, it considerably improved the ignitability of the compacts. Identification of the expelled substances would require further investigation including gas spectroscopy as well as X-ray diffraction of the substance collected on the walls of the reaction chamber.

The microstructure of the as-reacted sample shown in Fig. 3(a) illustrates the large amount of porosity present. It consists of large flaky voids along with smaller ones as shown in Fig. 3(b). Such porosity is due to the large volume change between reactants and products upon reaction as well as to the presence of entrapped gases, which are released and create channels during their trip to the surface of the sample. During reaction, the compact, with a starting density of $\approx 65\%$ of the theoretical reactant density, swells in the axial direction while no lateral expansion occurs, leaving the cylinder diameter at its initial value. The final density of the uncompacted sample is as low as 35% of the theoretical product density.

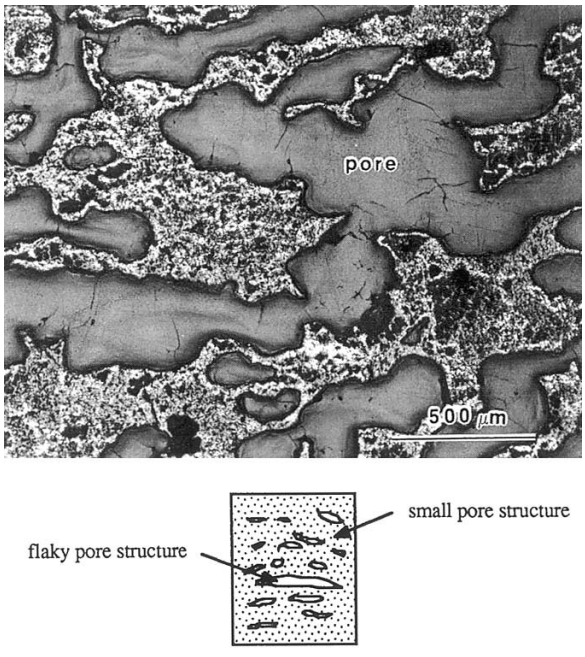

Fig. 3. (a) Porous microstructure of as-reacted TiB_2–Al_2O_3, and (b) schematic representation of the porosity distribution in the as-reacted compacts.

Overall, the combustion process seems to occur in a stable manner. This appears to be consistent with the reported literature, where unstable combustion of the reactant mixture has not been observed. As-reacted TiB_2–Al_2O_3 does not display a layered structure as was observed for the as-reacted TiB_2 samples obtained by Hoke et al. [23] resulting from an unstable pulsating combustion. The presence of a liquid phase during the synthesis may have prevented the appearance of such layers.

3.2. Consolidated compacts

The reacted and subsequently compacted TiB_2–Al_2O_3 samples display the same type of features with dynamic consolidation (DC) in a Dynapak high speed forging machine [22–25] and quasistatic consolidation (QC) in the Instron machine: cracks as well as porosity were present in all the samples. Final density ranges from 90% for the SHS/DC samples to a maximum of 95.7% for SHS/SC specimens.

Some preliminary consolidation tests were carried out with unconfined specimens. The absence of any lateral confinement usually provided by the containment assembly allowed the hot reacted material to flow laterally during compression; the resultant compacted samples displayed a low density, making the containment assembly a requirement to obtain high density values. Though the compacted material appeared to be in one piece after cooling in air, radial cracks were revealed during the removal of the top and bottom insulation layers. The explanation for the formation of cracks lies in thermal shock effects. A nonuniform distribution of the porosity, titanium diboride, and alumina phases was also observed as illustrated in Fig. 4. Three main regions are clearly identifiable in the cross-section of the sample:

- region I, formed by the upper part of the sample, where the ram acted, shows a relatively high density and a predominance of the titanium diboride phase;
- region II consists of the middle part of the compact and is characterized by the presence of a large amount of pores and a uniform distribution of the two phases;
- region III, which is mainly the bottom part of the sample, displays a high density and is alumina rich.

This seems to defy logic since TiB_2 is denser than $A1_2O_3$. However, after reaction, alumina is liquid while titanium diboride forms a rigid network. $A1_2O_3$ can

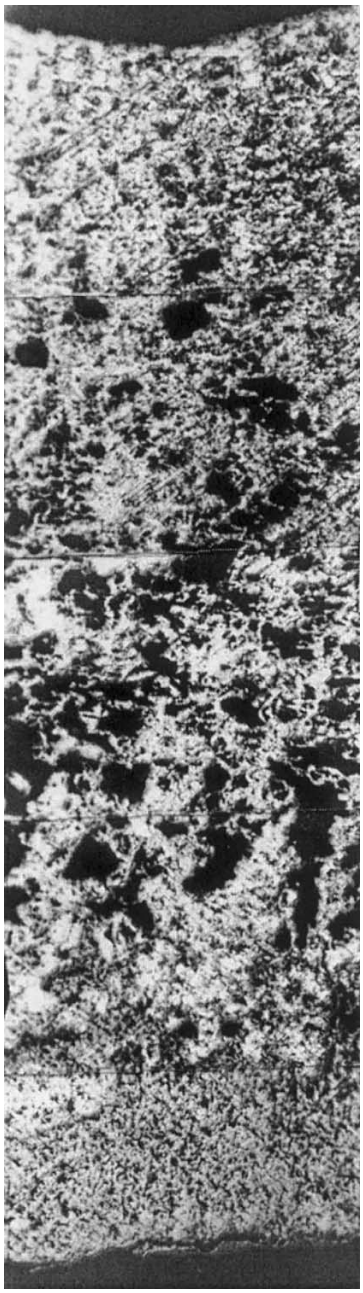

Fig. 4. Cross-section of reaction synthesized TiB_2–Al_2O_3 specimens compacted quasi-statically.

percolate down prior to densification and settle at the bottom of the sample while TiB_2 remains mainly at the top.

3.3. Thermal effects

The self-propagating synthesis of the TiB_2–Al_2O_3 material considered in this study is highly exothermic ($\Delta H = -297$ kJ/mol.). Following synthesis and compaction, the disk of material is cooled down inside its containment assembly by leaving it sitting in air. Heat flows from the hot material to the surrounding atmosphere. However, during the compaction step, following the end of the reaction synthesis, heat is transferred between the reacted compact and its surroundings. In the case of dynamic compaction, with ram velocities of up to 15 m/s, the process is fast enough to be considered isothermal. On the other hand, the quasi-static densification step lasts from several seconds to tens of seconds. Therefore, it cannot be considered isothermal.

The lateral, top and bottom surfaces of the material cool down while the center remains at a higher temperature. The effect of radiative and convective heat losses between the compact and the insulation layer as well as between the latter and the steel ring (which acts as a heat sink) are negligible compared to the heat flow due to conduction. Upon cooling, the outer part of the sample contracts because of its lower temperature thus creating a compressive state of strain in the center part. The inner material displays a higher temperature and retains its ductile state, which allows it to accommodate the strain. At this stage, the center of the specimen cools down and tends to contract; but the outer material, being rigid, does not accommodate the strain. This results in a tangential tensile stress. When these thermally induced stresses reach a critical value (the fracture strength of the material) and defects are present, cracks preferentially nucleate at defect sites in a direction perpendicular to that of the stress (radial cracks). Thermal stresses appearing during the nonuniform cooling as a result of temperature gradients inside the sample, can be evaluated using the first order relation given by Johns [28] and extended for brittle materials such as ceramics:

$$\sigma_{th} = E\alpha\Delta T \quad (2)$$

where α is the material thermal expansion coefficient; E is its Young's modulus, and ΔT is the temperature difference. In the TiB_2–Al_2O_3 composite, the ideal proportion of the phases is as follows: 73 vol.% $A1_2O_3$ and 27 vol.% TiB_2. The thermal expansion coefficient for the composite is calculated using a simple rule of mixture: $\alpha_c = 8.6 \times 10^{-6}$ °C^{-1}. The Young's modulus for the composite is approximately equal to 415 GPa. If one assumes a critical value for the formation of thermal cracks corresponding to the fracture strength of the material, it is possible to obtain an estimate of the temperature difference required to nucleate cracks. By considering tensile fracture strength for TiB_2–Al_2O_3 of 0.36 GPa, one obtains a minimum temperature difference of 100°C. Therefore, thermal gradients within the compact have to be avoided if cracking is to be eliminated.

An approximate calculation of the temperature variation with time inside the reacted and quasi-statically compacted TiB_2–Al_2O_3 disk is given here.

By assuming a very high value of the heat conductivity throughout the cooling of the unconfined TiB_2–

Al_2O_3 material (disk of 16 mm radius and 8 mm height), the temperature inside the sample can be considered uniform. Its variation with time can then be found by equating heat flow rates at the edge of the sample (conduction) and in the atmosphere surrounding the edge surface (convection). The resulting relation is given by:

$$T(t) = T_{rt} + (T_{ad} - T_{rt})\exp\left[-\frac{\bar{h}A_s}{\rho CV}t\right] \quad (3)$$

where T_{rt} and T_{ad} are respectively the room temperature ($T_{rt} = 25$°C) and the TiB_2–Al_2O_3 adiabatic temperature ($T_{ad} = 2175$°C). As is the sample edge surface area ($A_s = 2\pi r_0 h$, r_0 is the sample radius and h is the sample height); V is volume, and ρ and C are respectively the product density and heat capacity ($\rho = 4.12$ g/cm^3 and $C = 0.52$ J/g°C); $\bar{h}$ is the convection heat transfer coefficient given by the expression:

$$\bar{h} = \frac{T_{ad} - T_s}{T_s - T_{rt}}\frac{k_c}{r_0} \quad (4)$$

where k_c is the thermal conductivity of the composite at the surface ($k_c = 14.9$ W/m°C), r_0 is the sample radius ($r_0 = 16$ mm) and T_s is the outer surface temperature. T_s is assumed to be 1800°C as a first approximation since we can consider that the air in contact with the sample surface is heated up to that temperature. The relation governing the variation of temperature with time t at the edge of the sample is plotted in Fig. 5 and expressed as:

$$T(t) = 25 + 2150\exp[-0.0114t] \quad (5)$$

The results of Fig. 5 are approximate and were developed to provide a rough idea of the thermal behavior of the TiB_2–Al_2O_3 reacted and compacted samples.

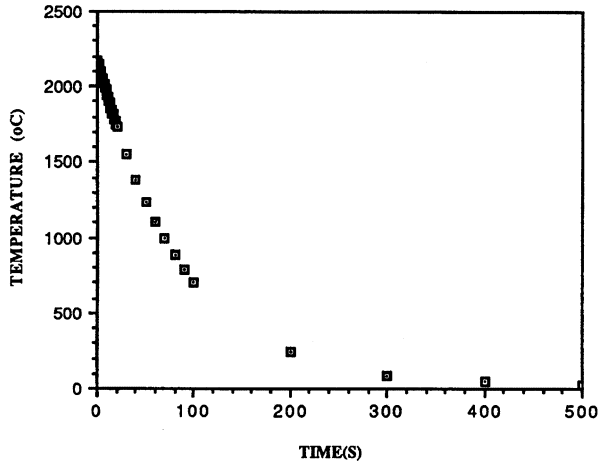

Fig. 5. Temperature as a function of time at the edge of an unconfined TiB_2–Al_2O_3 sample quasi-statically consolidated.

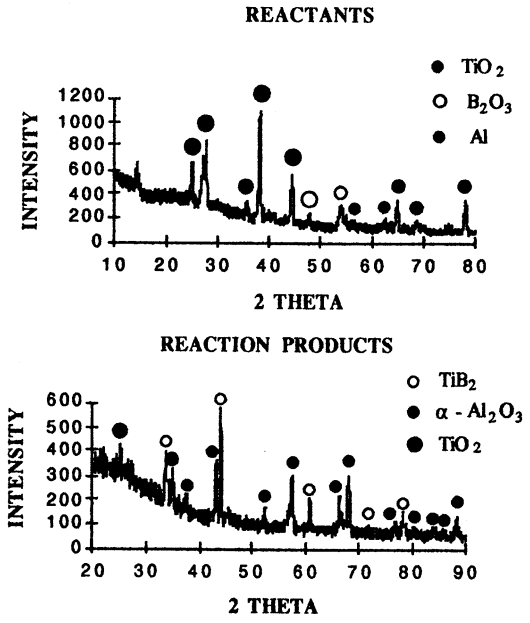

Fig. 6. X-ray diffraction spectra of (a) the reactant powders prior to synthesis, and (b) reaction synthesized TiB_2–Al_2O_3.

3.4. Characterization of the densified materials

3.4.1. Microstructures

The TiB_2–Al_2O_3 ceramic composite resulting from the combustion synthesis of the TiO_2–B_2O_3–Al system followed by compaction was observed to be a TiB_2 phase heterogeneously distributed in an $A1_2O_3$ matrix with the respective calculated proportions: TiB_2 (27 vol.%) and $A1_2O_3$ (71 vol.%). Fig. 6 shows the X-ray diffraction patterns of (a) the reactant powders and (b) the reaction products. In the reactants spectrum, the peaks corresponding to the starting materials are found: titanium dioxide, boron oxide and elemental aluminum. No trace of any impurity was detected. The reacted material spectrum displays the expected titanium diboride as well as alumina peaks corresponding to the α-Al_2O_3 polymorph. In the low angle region, a TiO_2 peak was identified, confirming the presence of a third phase observed by back scattering electron microscopy. It is thought to be unreacted titanium oxide.

Scanning electron microscopy (SEM) of the polished surfaces of typical (a) dynamically and (b) quasi-statically compacted TiB_2–Al_2O_3 samples is shown in Fig. 7. Back scattering detection mode was used on the SEM in order to enhance the phase contrast while observing polished samples. TiB_2 shows up as the bright regions while alumina forms the darker ones. The third phase, which appears even darker, represents the porosity distributed in the material. The inhomogeneous distribution of the phases can be noted. In Fig. 7(b), the presence of long and thin agglomerations of TiB_2 grains demonstrates the effect of compaction on the hot and ductile material. This also reveals the

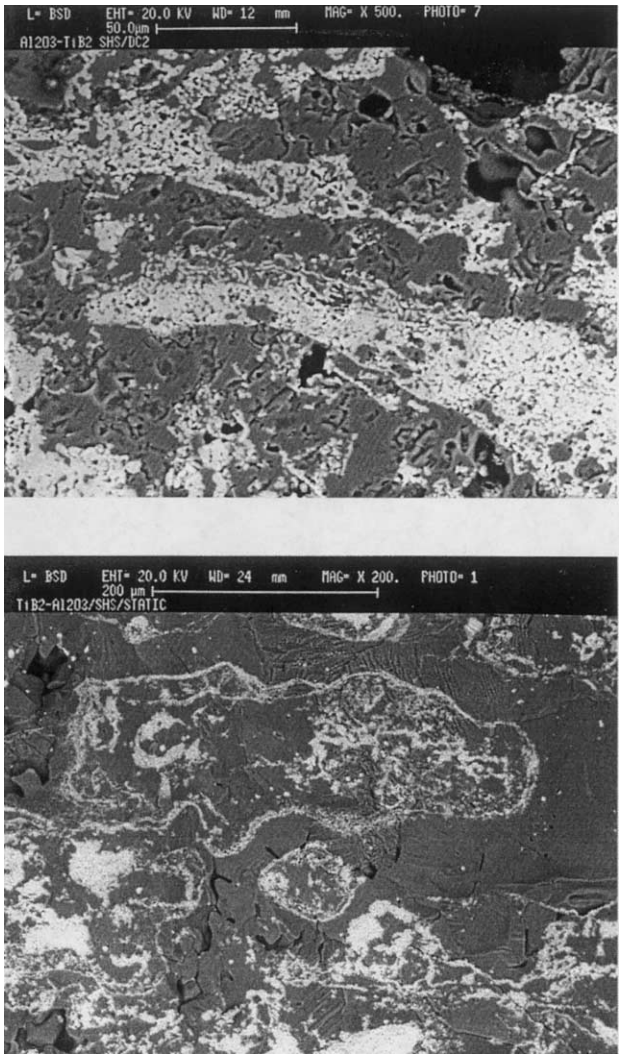

Fig. 7. Scanning electron micrographs of the polished surfaces of typical reaction synthesized TiB_2–Al_2O_3 followed by (a) dynamic compaction, and (b) quasi-static compaction.

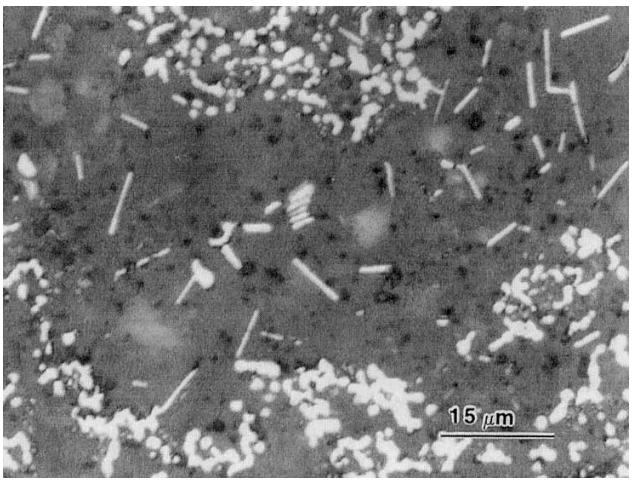

Fig. 8. Optical micrograph showing the dispersion of a needle shaped TiB_2 grains in the Al_2O_3 matrix.

inhomogeneity resulting from an incomplete dispersion of the reactant powders. While the alumina phase appears homogeneous, the TiB_2 phase is formed of clusters as well as what appears to be needle shaped grains or short fibers 5–10 μm long with a diameter of around 1 μm. These features are illustrated in Fig. 8 where two orientations can be seen. This might be explained by a growth from the melt, since, prior to the conversion to the products, all the reactants are in a liquid state. Assuming the reaction temperature to be the TiB_2–$A1_2O_3$ adiabatic temperature ($T_{ad} = 2175$°C), B_2O_3 melts first ($T_{mp} = 450$°C), followed by aluminum ($T_{mp} = 660$°C) and finally at 1830°C, TiO_2 becomes liquid. In that state, aluminum reduces both TiO_2 and B_2O_3 to yield elemental boron and titanium, which combine to give TiB_2. Along with the oxide reduction, aluminum oxidizes and $A1_2O_3$ is then formed. These needleshaped TiB_2 grains are formed during the reaction stage and are embedded into the large grained alumina phase during pore collapse due to densification. Fig. 9 shows a transmission electron micrograph of the TiB_2 phase in a TiB_2–Al_2O_3 quasi-statically compacted sample, where a mixture of needle shaped as well as rather equiaxed gains is clearly visible. If we assume a eutectic-type of growth for TiB_2 and $A1_2O_3$, the shape of the minor phase (TiB_2) can be predicted. According to Ashbrook [29], depending on the minor phase volume fraction, the eutectic microstructure may be rod-like or fibrous instead of lamellar during solidification of ceramic eutectics (directional or not): the

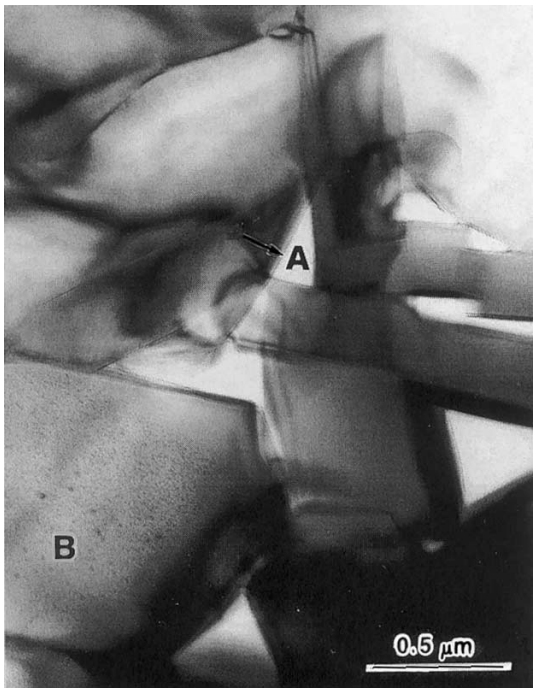

Fig. 9. Transmission electron micrograph of the TiB_2 general grain structure in quasi-statically compacted TiB_2–Al_2O_3. (A) inter-granular voids and (B) ion milling artifacts.

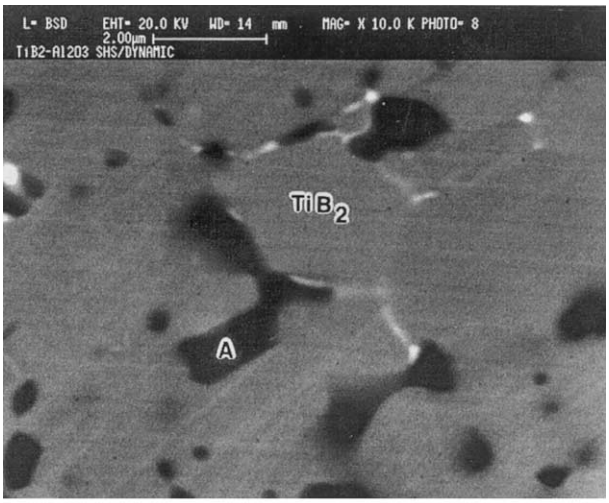

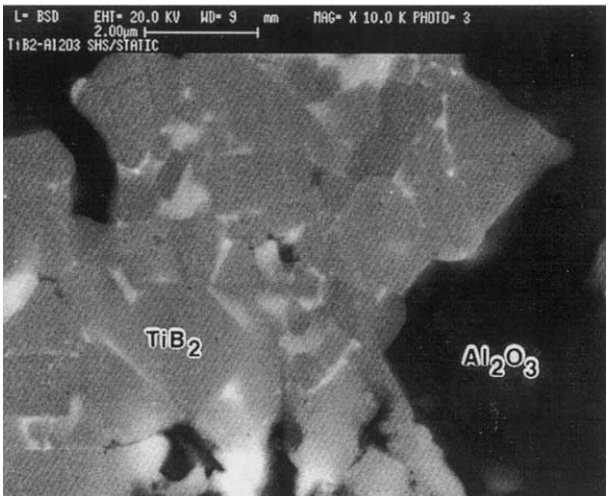

Fig. 10. Back scaffering electron micrographs of the TiB_2 grain structure in reacted TiB_2–Al_2O_3 followed by (a) dynamic compaction, and (b) quasi-static consolidation. The brightest phase is thought to be unreacted TiO_2. (A) represents pores.

transition from fibers to lamellae occurs for a volume fraction of $1/\pi$ (0.318). In our case, the volume fraction of TiB_2 is 0.27, leading to the observed needle-like structure. The white areas between grains are voids. Note the pores of angular shape (see arrow) and how the grains tend to be stacked with no boundary phase interaction.

The alumina phase displayed a much larger grain size in both type of samples: 20–50 μm depending on the observed region. In Fig. 10(b), the dark alumina phase surrounds the TiB_2 cluster. In both these micrographs, a brighter phase is present at some grain boundaries and triple points (see arrows). Given its brightness under back scattering electron microscopy, the unidentified material is assumed to be heavier than TiB_2 as a compound. After cross checking information on the EDS detector, the phase was deduced to contain titanium. Based on the X-ray data, where a TiO_2 peak was identified, this phase is believed to be unreacted TiO_2.

Two types of porosity were observed in the TiB_2 phase (inter- and intra-granular) as can be seen in Fig. 10(a) and (b). The great amount of shrinkage during conversion of the reactants ($\Delta V = 28\%$) is the main source of intrinsic porosity to be added to the initial porosity from the green compact. While the open porosity present at the TiB_2 grain boundaries may be attributed to the incomplete collapse of the initial pore structure during the densification step due to an insufficient compacting force, the closed intra-granular voids are due to the presence of trapped reaction gases, which were not expelled during the later stages of synthesis and densification.

The presence of a liquid phase during the reaction process is illustrated by some features in both Al_2O_3

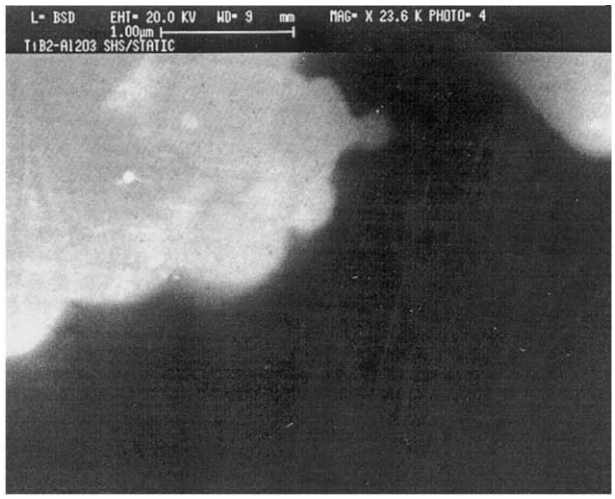

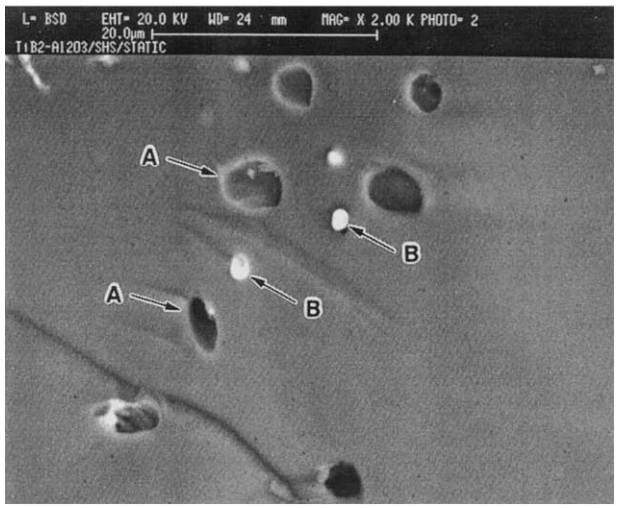

Fig. 11. (a) High magnification back scattering electron micrograph of the TiB_2/Al_2O_3 interface in quasi-statically compacted TiB_2–Al_2O_3 illustrating the presence of liquid phase during synthesis. (b) Back scattering electron micrograph of the Al_2O_3 phase of a quasi-statically compacted TiB_2–Al_2O_3 sample displaying intra-granular voids and isolated TiB_2 grains.

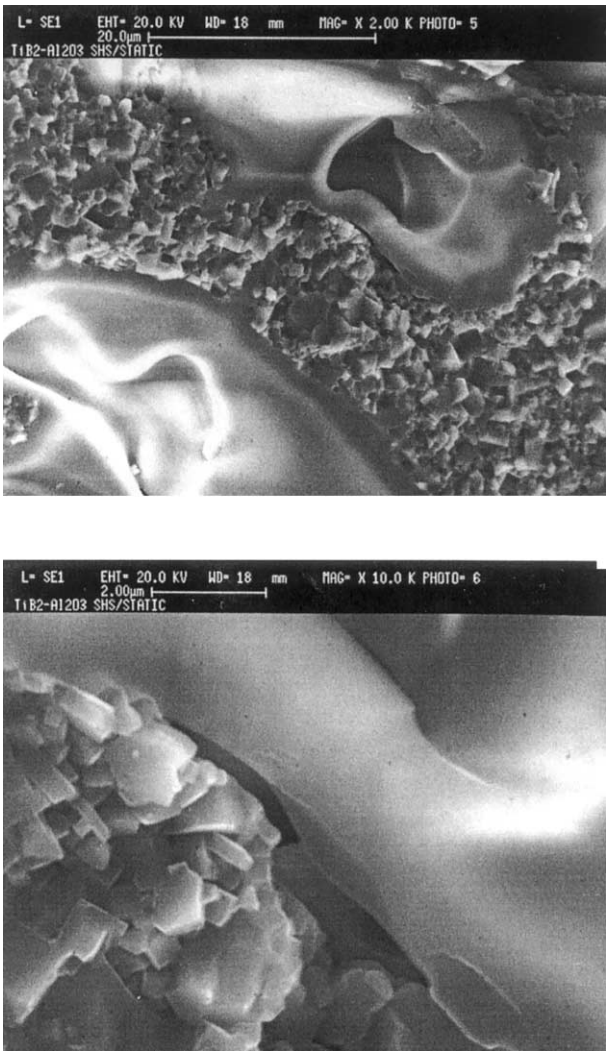

Fig. 12. Scanning electron micrographs of the TiB_2/Al_2O_3 interface region showing no wetting between the two phases (a) general view of the two phases, and (b) close up of the interface region.

and TiB_2 grain structures. Fig. 11(a) shows a high magnification scanning electron micrograph of the TiB_2/Al_2O_3 interface. The round shape of TiB_2 grains at the interface results from an isotropic surface energy distribution during grain growth which follows the compaction step, that may be an evidence of the presence of molten alumina during growth of the TiB_2 gains. Growth of TiB_2 grains is believed to happen after the consolidation step because of their rather smooth features and low dislocation densities. As shown in Fig. 11(b), (Arrow A), the alumina intra-granular porosity displays a spherical shape that can be attributed to the presence of a liquid phase. These spherical pores result from the gases entrapped during the reaction process as was explained for the similar cases of voids located within the interior of TiB_2 gains. Isolated bright TiB_2 gains are found in the Al_2O_3 phase illustrated in Fig. 11(b). Their round features correspond to the section of whisker shaped grains perpendicular to their elongated direction (Arrow B).

The TiB_2/Al_2O_3 interface shown in Fig. 11(a) confirmed the presence of a liquid phase during reaction synthesis. The scanning electron micrograph shown in Fig. 12 reveals voids separating the small grained TiB_2 phase from the larger gained Al_2O_3 phase. The presence of such features tends to prove that alumina incompletely wets titanium diboride.

The overall microstructure displays few dislocations which are always located in the TiB_2 grains as shown in Fig. 13. This may be explained by the fact that reacted TiB_2 is in a solid ductile state just after synthesis and is allowed to anneal because of its high temperature. Annealing reduces the dislocation density formed during the compaction step where TiB_2 grains plastically deformed in response to the compressive load. No dislocations were observed in the alumina phase.

3.4.2. Microhardness

Vickers microhardness tests were performed on the densified material. Because of the presence of two distinct phases, the hardness across a section of the material oscillates around two distinct values. Important variations around the respective mean hardness values of the phases also occur due to the porosity present in the specimens. A decrease in the oscillation amplitude is expected to accompany an increase in relative density due to reduced effects of porosity. Less porosity increases the chance to place the Vickers indenter in a

Fig. 13. Transmission electron micrograph of a dislocation array located within a TiB_2 grain in quasi-statically consolidated TiB_2–Al_2O_3.

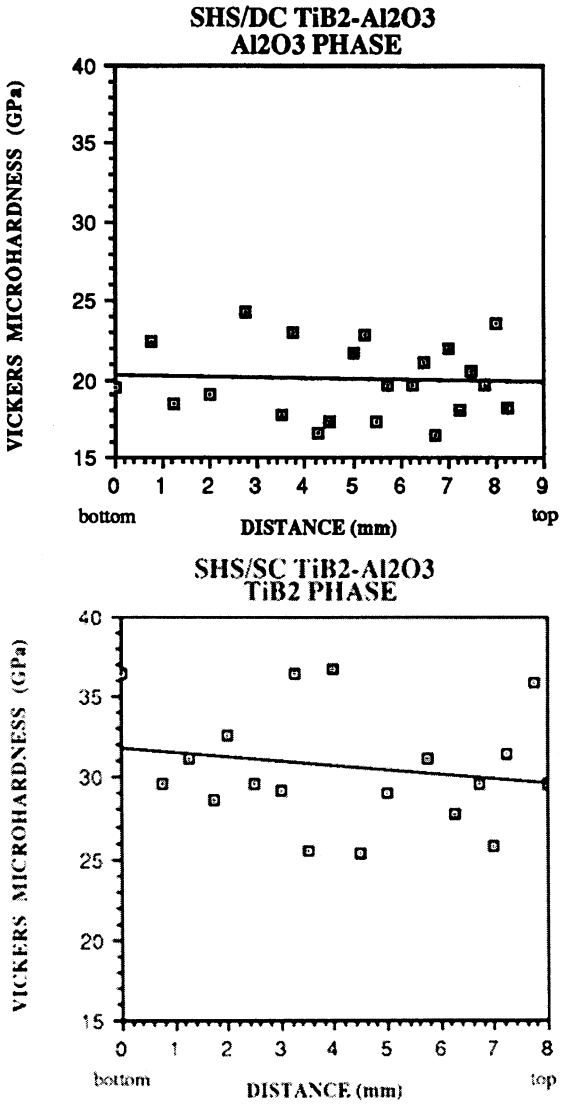

Fig. 14. Vickers microhardness of (a) the Al_2O_3 phase, and (b) the TiB_2 phase within cross-sections of a TiB_2–Al_2O_3 composite sample.

Table 1
Initial strain rates used to quasi-statically consolidate reacted TiB_2–Al_2O_3 according to the Instron machine crosshead velocity and specimen height

Cross-head velocity (mm/min)	177.8	127.0	58.4	25.4
Specimen height (mm)	Strain rates (S^{-1})			
10	N/A	2.1×10^{-1}	N/A	N/A
13	N/A	1.6×10^{-1}	N/A	N/A
19	1.5×10^{-1}	1.1×10^{-1}	4.4×10^{-2}	2.2×10^{-2}
38	7.8×10^{-2}	5.5×10^{-2}	2.2×10^{-2}	1.1×10^{-2}

pore free region and then avoid the risk to see the material collapse under the load because it was applied at a point too close to a porous region. Fig. 14(a) shows the variation of microhardness in the TiB_2 phase across the section while Fig. 14(b) examines the $A1_2O_3$ phase under the same conditions. Average hardness of the TiB_2 phase was approximately 30.6 GPa $\pm$ 3.6, while the $A1_2O_3$ phase displays an average microhardness of 20.7 GPa $\pm$ 3.1. The average hardness values obtained for the TiB_2 phase seem to be relatively high compared to the one reported by Hoke et al. [23] (22.0 GPa $\pm$ 6.4) but the value of 33.3 GPa mentioned in the literature falls within the standard deviation range of the two experimental values reported above. The microhardness values, found in the literature for α-alumina are around 20 GPa, which agrees with the present experimental data. The average hardness of TiB_2–Al_2O_3 can be obtained with respect to the volume percentage of each phase (73 vol.% $A1_2O_3$ and 27% TiB_2). The calculated values is 23.4 GPa $\pm$ 3.2. This value is very close to the 21.6 GPa value reported by Cameron et al. [6] for Vickers hardness of the same TiB_2–Al_2O_3 material synthesized by SHS followed by hot-pressing.

3.5. Consolidation behavior of SHS/SC TiB_2–Al_2O_3

The study of the densification behavior of reacted TiB_2–Al_2O_3 was conducted at strain rates ranging from 1.1×10^{-2} S^{-1} to 1.1×10^{-1} S^{-1} by varying crosshead velocities (25.4–50.8–127.0–177.8 mm/min) and sample heights (10–13–19–38 mm). Following reaction synthesis, the material displays a very high temperature ($T_{ad}=2175$°C) and immediately starts cooling down as was seen in Section 3.3 and Fig. 5. Therefore, the quasi-static densification process cannot be considered isothermal since consolidation time ranges from 8 s up to 50 s and the decrease in temperature is quite substantial ($\Delta T=300$–600°C as seen in Fig. 5). The load–time curves then combine both the densification and cooling effects. At high temperature, the reacted material is in a global ductile state and stiffens while cooling down, ultimately reaching its ductile/brittle transition temperature. During densification of the porous material, while it still is in a ductile state, the stress given by the curves corresponds to the flow stress of the material. The temperature effect was incorporated into the axial flow stress versus density curves based on four theoretical models for the rigid-plastic [31–34] and power-law creep [30,33,34,37] densification behavior of porous materials (powder compacts).

3.5.1. Consolidation and stress–strain curves

Since the testing machine operates at a constant cross-head velocity, strain rate is not a constant during the test. Table 1 gives the initial strain rates used for the experiments in accordance with the machine velocity and height of the sample.

Some experimental features must be taken into consideration. After ignition, the reaction wave propagates down through the contained sample, which expands in the axial direction. The initial density of the reacted sample is decreased prior to compaction (down to 30% of the product density). The actual total displacement during compression can therefore exceed the initial height of the sample. Moreover, the displacement due to the stiffness of the machine (frame and fixtures) was taken into consideration for the elaboration of stress–density and stress–strain curves.

A typical stress versus density plot for the densification of TiB_2–Al_2O_3 is shown in Fig. 15(a). Three distinct densification regions can be identified. At first, the increase in density at very low values of stress corresponds to both compression of the loose powder added for ignition on top of the sample and the collapse of the large flaky pore structure at high temperature (region I). The slope of this range is very low. A schematic illustration of the porosity shape and distribution inside uncompacted specimens is given in Fig. 3(b). In an intermediate stage (region II), stress starts increasing regularly with density. This region can be attributed to the end of the collapse of the largest pores combined with the beginning of smaller pore elimination while temperature is decreasing. The final stage (region III) corresponds to the collapse of the small pore structure accompanied by stiffening of the bulk material (temperature drops due to heat losses). In that region, stress dramatically increases when density reaches high values.

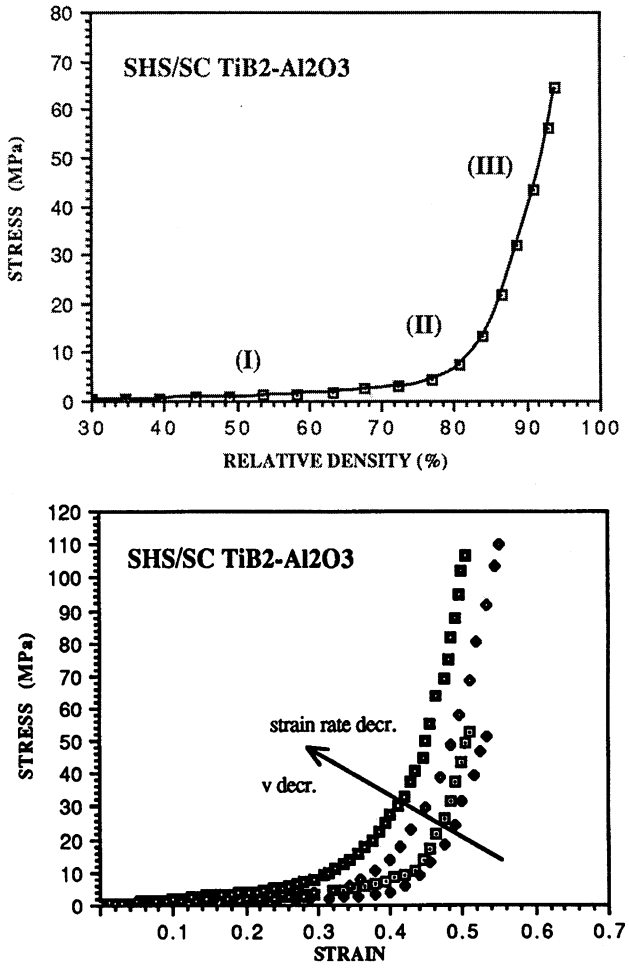

Fig. 15. (a) Typical stress-density curve for the consolidation of TiB_2–Al_2O_3. (b) Stress–strain curves for quasi-static compaction of TiB_2–Al_2O_3 samples showing the effect of strain rate.

The stress–strain curves corresponding to quasi-static compaction of reacted TiB_2–Al_2O_3 show the same general shape as the stress–density ones. The effect of strain rate can be clearly seen in Fig. 15(b) where the slope of the stress–strain curve increases with decreasing values of strain rate. Tests at lower strain rate last longer, implying more heat losses, a lower temperature, and attendant stiffening of the material. Stress therefore reaches a higher value for the same amount of strain.

3.5.2. Constitutive models

The purpose of this section is to model the behavior of ductile SHS/SC TiB_2–Al_2O_3 during quasi-static consolidation. By comparing the observed and predicted uniaxial strain compression behavior (using modified densification models of the hot porous material in which a temperature dependent flow stress is incorporated), it is possible to obtain a preliminary value and to approximate the variation of the flow stress of porous TiB_2–Al_2O_3 with temperature.

3.5.2.1. Model of rigid-plastic constitutive behavior for densification of porous materials. The general expression of the yield criterion for ductile porous materials in an isothermal experiment is given by [32]:

$$\frac{P^2}{\psi}+\frac{\tau^2}{\varphi}=\delta\sigma_{y_0}^2 \tag{6}$$

where different expressions have been proposed for φ, ψ and δ in terms of relative density ρ. τ is the second invariant of deviatoric stress component and P, the first invariant of the stress tensor. σ_{y_0} is the yield stress of the fully dense material. For the specific case of uniaxial strain compression (repressing) of an axisymmetric body, it is assumed that $d\varepsilon_r = d\varepsilon_\theta = 0$ and $\sigma_r = \sigma_\theta = [\nu/(1-\nu)]\sigma_Z$ (ν being Poisson's ratio of the material). The stress tensor invariant are then given by:

$$P=\frac{\sigma_r+\sigma_\theta+\omega_Z}{3}=\frac{1}{3}\left(\frac{1+\nu}{1-\nu}\right)\sigma_Z \tag{7}$$

Table 2
Expression of parameters A, B and δ for Skorohod, Kuhn and Downey, Gurson and Doraivelu models

Models	φ	ψ	δ
Skorohod	$\frac{1}{\rho^2}$	$\frac{3}{2}\frac{(1-\rho)}{\rho^3}$	ρ
Kuhn and Downey	$\frac{3}{2}\rho(2+\rho^2)$	$\frac{9}{2}\rho(3-\rho)(1-\rho)$	ρ
Gurson (approximation obtained in [31])	$\frac{9}{2}\frac{1-(1-\rho)^2}{1+(1-\rho)^3}$	$\frac{9}{2}\frac{(1-\rho)^2(1-(1-\rho)^2)}{1+(1-\rho)^3}$	ρ
Doraivelu	$\frac{3(2+\rho^2)}{2(2\rho^2-1)}$	$\frac{9(3-\rho)(1-\rho)}{2(2\rho^2-1)}$	1
McMeeking and Sofronis	$\left(\frac{\rho}{2-\rho}\right)^{\frac{2}{m+1}}$	$\frac{2}{3}\left(\frac{1-(1-\rho)^m}{m(1-\rho)^m}\right)^{\frac{2}{m+1}}$	ρ

$$\tau=\frac{1}{3}[(\sigma_r-\sigma_\theta)^2+(\sigma_\theta-\sigma_z)^2+(\sigma_z-\sigma_r)^2]$$
$$=\frac{2}{3}\left(\frac{1-2\upsilon}{1-\upsilon}\right)^2\sigma_z^2 \quad (8)$$

where σ_Z is the axial stress.

There exist a substantial number of model describing coefficients φ, ψ and δ as function of the relative density ρ. Here we consider four models of Kuhn and Downey [30], Gurson [33], Skorohod [34] and Doraivelu et al. [31]. Table 2 shows the corresponding values of parameters φ, ψ and δ for these models.

For porous materials, Kuhn and Downey [30] found the relationship between ρ and ν to be $\rho^2=2\nu$. In the model they proposed, $\varphi=\frac{2}{(2+\rho^2)}$, $\psi=\frac{1}{3(1-\rho^2)}$, and $\delta=1$. The yield criterion is then given by:

$$\sigma_z(\rho)=\sigma_{y_0}\left[\frac{(2-\rho^2)}{(1-\rho^2)(2+\rho^2)}\right]^{\frac{1}{2}} \quad (9)$$

On the other hand, Doraivelu et al. [31] introduced the dependence of yield stress on relative density via a δ term:

$$\delta=\frac{\rho^2-\rho_i^2}{1-\rho_i^2} \quad (10)$$

According to that model, the critical density (ρ_c) where the compact looses all mechanical strength was chosen to be the density at the beginning of consolidation, $\rho_c\approx 0.4$ (40% of the products theoretical density). Such a choice was made because of the presence of a liquid phase during the reaction ($T_{ad}=2175$°C) and the first stage of compaction (before solidification of the alumina phase at $T_{am}=2080$°C). Expressions for the axial stress (σ_Z) as a function of density during uniaxial strain densification (repressing) experiments is then given by corresponding four above-mentioned models as: (see Table 2 for corresponding φ, ψ and δ in terms of relative density ρ)

Doraivelu:

$$\sigma_Z=-\sigma_{y_0}\left(\frac{\rho^2-\rho_i^2}{1-\rho_i^2}\right)^{\frac{1}{2}}\left(\frac{2-\rho^2}{(1-\rho^2)(2+\rho^2)}\right)^{\frac{1}{2}} \quad (11a)$$

Kuhn and Downey:

$$\sigma_Z=-\frac{\sqrt{2}}{3}\sigma_{y_0}\left(\frac{2}{2+\rho^2}+\frac{1}{(1-\rho)(3-\rho)}\right)^{\frac{1}{2}} \quad (11b)$$

Skorohod:

$$\sigma_Z=-\sqrt{\frac{2}{3}}\sigma_{y_0}\frac{\rho^{\frac{3}{2}}}{(1-\rho)^{\frac{1}{2}}} \quad (11c)$$

Gurson:

$$\sigma_Z=-\frac{\sqrt{2}}{3}\sigma_{y_0}\frac{1}{1-\rho}\left[(\rho+(1-\rho)^2)\frac{2(1-\rho)^2+1}{3}\right]^{\frac{1}{2}} \quad (11d)$$

These expressions remain valid as long as the experiment is isothermal. However, the consolidation process at low strain rate cannot be considered as isothermal. A temperature dependence must therefore be added to Eqs. (11a), (11b), (11c) and (11d) and σ_{y_0} has to be replaced by a temperature dependent term $\sigma_y(T)$. As a first approximation, it is assumed that the dependence of yield stress on temperature is given by:

$$\sigma_y(T)=\sigma_{y_0}\left(1-\frac{T-T_0}{T_{am}-T_0}\right) \quad (12)$$

where σ_{y_0} is a 'pseudo' yield stress at $T_0=25$°C, the room temperature. Since the liquid alumina phase exists until $T_{am}=2080$°C, the flow stress can be assumed to be zero between the adiabatic temperature T_{ad} and T_{am}.

The stress-density relationship describing the hot porous material behavior during consolidation that includes the effect of temperature is obtained by substituting Eq. (12) into the modified form of Eqs. (11a), (11b), (11c) and (11d):

Doraivelu:

$$\sigma_Z(\rho,T) = -\sigma_{y_0}\left(1-\frac{T-T_0}{T_{am}-T_0}\right)\left(\frac{\rho^2-\rho_i^2}{1-\rho_i^2}\right)^{\frac{1}{2}}\left[\frac{(2-\rho^2)}{(1-\rho^2)(2+\rho^2)}\right]^{\frac{1}{2}} \quad (13a)$$

Kuhn and Downey:

$$\sigma_Z = -\frac{\sqrt{2}}{3}\sigma_{y_0}\left(1-\frac{T-T_0}{T_{am}-T_0}\right)\left(\frac{2}{2+\rho^2}+\frac{1}{(1-\rho)(3-\rho)}\right)^{\frac{1}{2}} \quad (13b)$$

Skorohod:

$$\sigma_Z = -\sqrt{\frac{2}{3}}\sigma_{y_0}\left(1-\frac{T-T_0}{T_{am}-T_0}\right)\left[\frac{\rho^{\frac{3}{2}}}{(1-\rho)^{\frac{1}{2}}}\right] \quad (13c)$$

Gurson:

$$\sigma_Z = -\frac{\sqrt{2}}{3}\sigma_{y_0}\frac{1}{1-\rho}\left(1-\frac{T-T_0}{T_{am}-T_0}\right)\left[(\rho+(1-\rho)^2)\frac{2(1-\rho)^2+1}{3}\right]^{\frac{1}{2}} \quad (13d)$$

Eqs. (13a), (13b), (13c) and (13d) depend explicitly on temperature and density, and also implicitly on time via T and ρ. The temperature as a function of time was obtained in Section 3.3 with Eq. (5) (where T is expressed in °C and t in seconds).

The relative density as a function of time, ρ(t), is obtained by considering the decrease of the height (initial height h_0' after axial expansion due to reaction) of the cylindrical samples during consolidation, assuming a constant diameter (cross-section area A) at a given crosshead velocity (v) and mass sample (M); the theoretical density of the TiB_2–Al_2O_3 products is ρ_P ($\rho_P = 4.12$ g/cm^3):

$$\rho(t) = \frac{M}{\rho_P A(h_0' - vt)} \quad (14)$$

The time elapsed during cooling from T_{ad} to T_{am} ($\Delta t = 4$ s) has to be subtracted from the total experimental time. The σ_{y_0} value was adjusted in order to match the experimental curves; shown in Fig. 16(a), where both the four models and experiment are repre-

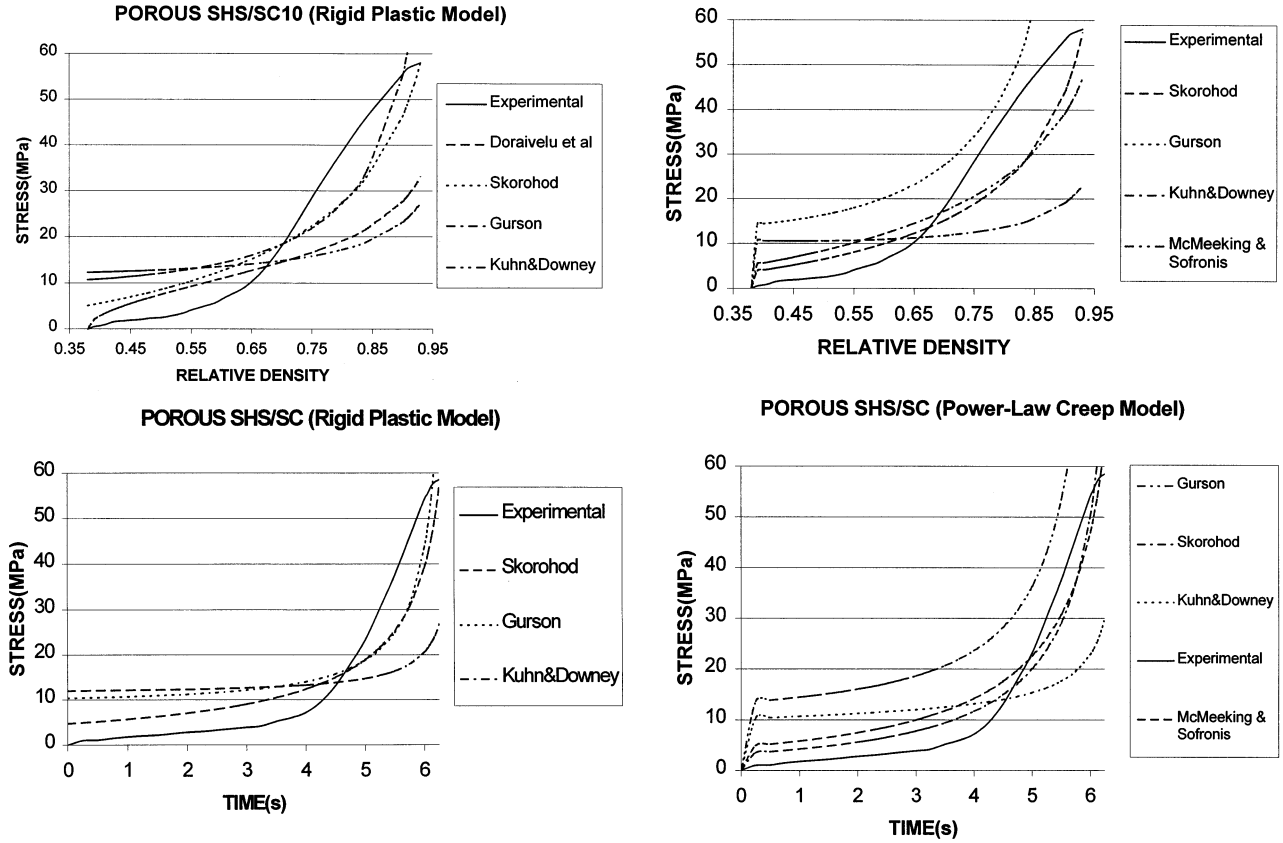

Fig. 16. Comparison of the constitutive models for axial strain compression (repressing) of hot porous TiB_2–Al_2O_3 and the corresponding experimental curve. (a) Stress versus relative density (rigid plastic), (b) stress versus time (rigid plastic), (c) stress versus relative density (power-law creep) and (d) stress versus time (power-law creep).

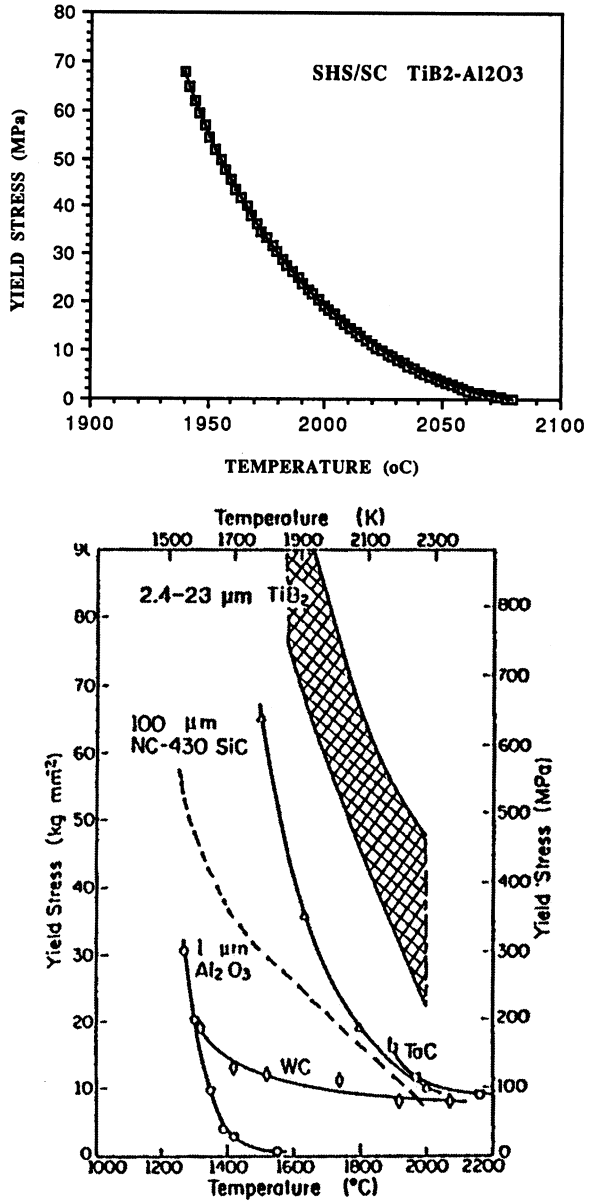

Fig. 17. (a) Yield stress as a flinction of temperature for TiB_2–Al_2O_3 during quasi-static consolidation. (b) Summary of high temperature yields stress data for several structural ceramics [31]. The dashed line represents an interpolation of the data for the TiB_2–Al_2O_3 composite (rule of mixtures).

sented. For the respective values of the test parameters ($M = 27$ g, $A = 7.9$ cm^2, $h'_0 = 2.2$ cm, $v = 0.212$ cm/s, $\rho_i = 0.37$, $\rho_{final} = 0.932$ and $t_{final} = 10.2$s, ($\sigma_{z.max} = 60$ MPa), the 'pseudo' yield stress σ_{y_0} that best matches the experimental results in the experiment of Doraivelu et al. [31] model is 1.07 GPa. The evolution of the yield stress within the temperature range of the quasistatic consolidation experiments (1940–2175°C) is shown in Fig. 17(a).

Ramberg and Williams [35] reported the yield stresses of TiB_2 and Al_2O_3 as a function of temperature, as can be seen in Fig. 17(b). Superimposed on the data of Fig. 17(b), a dashed line was added representing a rule of mixtures yield stress for 27 vol.% TiB_2–73 vol.% Al_2O_3 mixture. By comparing Fig. 17(a) and (b), it is seen that the value obtained from the model developed here is fairly consistent with the results interpolated from Ramberg and Williams [35].

The value for σ_{y_0} that fits the experimental results best is somewhat artificial, because TiB_2 and Al_2O_3 do not undergo plastic deformation at room temperature and fail by fracture. The compressive strength of this TiB_2–Al_2O_3 composite would be closer to 4 GPa.

The results of calculations in accord with four models (Gurson, Skorohod, Kuhn and Downey and Doraivelu et al.) are compared to the experimental data on (axial) stress–relative density and (axial) stress–time dependencies on Fig. 16(a,b).

We can see that the better fit is provided by Skorohod and Gurson models, however, for all the models applied, the deviation from the experimental data is rather substantial. This can be explained by the fact that all the above mentioned models are based on the idea of rigid-plastic material behavior. However, it is shown [36] that for most hot-pressing processes, the dominant mechanism of material flow is power-law creep.

It is noteworthy, that the rigid-plastic models assume an initial stress threshold (initial non-zero yield stress) at the initial moment of time. On the contrary, power-law creep results in a zero stress level, when strain rate is equal to zero in the beginning of pressing (see Fig. 16c,d).

The only exception is the model of Doraivelu et al., where Eq. (10) is employed in order to satisfy the initial zero-stress requirement (observed in experiment) for the originally rigid-plastic model of porous material behavior. Physically Eq. (10) means the requirement for initial yield stress to be equal to zero (when $\rho = \rho_i$). Thereby, being originally rigid-plastic, the model of of Doraivelu et al. attempts to impose some elements of material behavior characteristic for power-law creep. However, one can see from Fig. 16(a,b), that this model, as well as other models of rigid-plastic behavior, cannot satisfactorly describe hot-pressing of a powder material in a rigid die.

3.5.2.2. Power-law creep model for densification of porous materials. The mechanical response of a nonlinear-viscous porous body obeying a power-law creep mechanism of material flow can be described [34] by a rheological (constitutive) relationship connecting components of stress tensor σ_{ij} and strain rate tensor $\dot{e}_{ij}$:

$$\sigma_{ij} = A\left(\frac{\sqrt{\varphi\dot{\gamma}^2 + \psi\dot{e}^2}}{\sqrt{\rho}}\right)^{m-1}\left[\varphi\dot{e}_{ij} + \left(\psi - \frac{1}{3}\varphi\right)\dot{e}\delta_{ij}\right] \quad (15)$$

where φ and ψ are the shear and bulk viscosity moduli

(see Table 2), which depend on relative density ρ (for example, following [34], $\varphi = \rho^2$, $\psi = \frac{2}{3}\frac{\rho^3}{(1-\rho)}$); δ_{ij} is a Kronecker symbol ($\delta_{ij} = 1$ if $i = j$ and $\delta_{ij} = 0$ if $i \neq j$); $\dot{e}$ is the first invariant of the strain rate tensor, i.e. sum of tensor diagonal components: $\dot{e} = \dot{e}_{11} + \dot{e}_{22} + \dot{e}_{33}$. Physically, $\dot{e}$ represents the volume change rate of a porous body.

Parameter $\dot{\gamma}$ is the second invariant of the strain rate tensor deviator and represents, physically, the shape change rate of a porous body:

$$\dot{\gamma} = \left[\left(\dot{e}_{ij} - \frac{1}{3}\dot{e}\delta_{ij}\right)\left(\dot{e}_{ij} - \frac{1}{3}\dot{e}\delta_{ij}\right)\right]^{1/2} \tag{16}$$

Physically, $\dot{\gamma}$ represents the shape change rate of a porous body. The strain rate sensitivity m varies in range $0 < m < 1$. In one limiting case, when $m = 1$, one obtains the equation corresponding to the behavior of a linear-viscous porous body:

$$\sigma_{ij} = A\left[\varphi\dot{e}_{ij} + \left(\psi - \frac{1}{3}\varphi\right)\dot{e}\delta_{ij}\right] \tag{17}$$

If $m = 0$, the equation corresponding to a rigid-plastic porous body is obtained:

$$\sigma_{ij} = \frac{A\sqrt{\rho}}{\sqrt{\varphi\dot{\gamma}^2 + \psi\dot{e}^2}}\left[\varphi\dot{e}_{ij} + \left(\psi - \frac{1}{3}\varphi\right)\dot{e}\delta_{ij}\right] \tag{18}$$

Here A plays the role of a yield stress σ_{y_0} of a fully-dense material in Eqs. (6), (9), (11a), (11b), (11c), (11d), (12), (13a), (13b), (13c) and (13d).

Eqs. (11a), (11b), (11c) and (11d) and Eqs. (13a), (13b), (13c) and (13d) could be derived by direct substitution of the corresponding φ, ψ, (taking into account that $\delta = \rho$) in Eq. (18).

In case of uniaxial pressing in a rigid die, $\dot{\gamma} = \sqrt{\frac{2}{3}}|\dot{\varepsilon}_Z|$ and $\dot{e} = \dot{\varepsilon}_Z$. Then Eq. (15) can be reduced to:

$$\sigma_Z = -A\frac{\left(\frac{2}{3}\varphi + \psi\right)^{\frac{m+1}{2}}}{\rho^{\frac{m-1}{2}}}\dot{\varepsilon}_Z^m \tag{19}$$

Here we use the expressions for φ and ψ corresponding to four different models: Gurson, Skorohod, Kuhn and Downey, and McMeeking–Sofronis [37] (see Table 2).

Since the consolidation process is conducted at low strain rate, in general, it cannot be considered as isothermal. We introduce ths same temperature dependence term $\sigma_y(T)$ as in Eq. (12). Then, the stress-density relationship describing the hot porous material behavior during consolidation that includes the effect of temperature by using power-law creep material behavior, can be obtained for the four above-mentioned models. Thus we have:

Gurson:

$$\sigma_Z(\rho,T) = -A\left(1 - \frac{T - T_0}{T_{am} - T_0}\right)\frac{\left[\frac{4}{27}\frac{(1+(1-\rho)^3)}{(1-(1-\rho)^2)} + \frac{2}{9}\frac{(1+(1-\rho)^3)}{(1-(1-\rho)^2)(1-\rho)^2}\right]^{\frac{m+1}{2}}}{\rho^{\frac{m-1}{2}}}\dot{\varepsilon}_Z^m \tag{20a}$$

Skorohod:

$$\sigma_Z(\rho,T) = -A\left(1 - \frac{T - T_0}{T_{am} - T_0}\right)\rho^{\frac{m+3}{2}}\left[\frac{2}{3} + \frac{2}{3}\frac{\rho}{(1-\rho)}\right]^{\frac{m+1}{2}}\dot{\varepsilon}_Z^m \tag{20b}$$

Kuhn and Downey:

$$\sigma_Z(\rho,T) = -A\left(1 - \frac{T - T_0}{T_{am} - T_0}\right)\frac{\left[\frac{4}{9\rho(2+\rho^2)} + \frac{2}{9\rho(1-\rho)(3-\rho)}\right]^{\frac{m+1}{2}}}{\rho^{\frac{m-1}{2}}}\dot{\varepsilon}_Z^m \tag{20c}$$

McMeeking and Sofronis:

$$\sigma_Z(\rho,T) = -A\left(1 - \frac{T - T_0}{T_{am} - T_0}\right)\frac{\left[\frac{2}{3}\left(\frac{\rho}{2-\rho}\right)^{\frac{2}{m+1}} + \frac{2}{3}\left(\frac{1-(1-\rho)^m}{m(1-\rho)^m}\right)^{\frac{2}{m+1}}\right]^{\frac{m+1}{2}}}{\rho^{\frac{m-1}{2}}}\dot{\varepsilon}_Z^m \tag{20d}$$

At the same time, we have the following expression for the axial strain rate for rigid die compressing:

$$\dot{\varepsilon}_Z = \frac{\dot{h}}{h} = \frac{\Delta h/\Delta t}{h} = \frac{V}{h_i - Vt} \tag{21}$$

where $\dot{h}$ is the height change rate of the specimen, h is the height of the specimen, h_i is the current height of the specimen, V is the moving speed of the punch, which is known for a specific experiment.

And for the porosity, since the mass of the specimen is conserved during the test $\rho V_s = const$ (where V_s is the specimen's volume), we have the following expression:

$$\rho V_s = \rho\pi r^2 h = \rho_i\pi r^2 h_i = \rho_i V_i \Rightarrow \rho = \rho_i\frac{h_i}{h} = \rho_i\frac{h_i}{h_i - vt} \tag{22}$$

where ρ is the current porosity and ρ_i and V_i are the initial porosity and volume of the specimen, respectively.

Substituting Eq. (21) and Eq. (22) into Eqs. (20a–d),

we can get the axial stress σ_Z as a function of time t and temperature T.

The results of the calculations in accord with Eqs. (20–22) are given in Fig. 16(c–d).

One can see, that the power-law creep relationships (24) (Fig. 16c–d) provide with better agreement with the experimental data than the rigid-plastic models (13) (Fig. 16a–b). The best fit corresponds to the Skorohod [34] and McMeeking–Sofronis [37] models. A conducted regression analysis shows that the best agreement with the experiment is achieved when $A = 1$ (GPa $s^{0.3}$) and $m = 0.3$.

While the McMeeking–Sofronis model has been specifically designed for the power-law creep behavior of porous materials, one should note the 'average' character of the Skorohod model which provides reasonable results for a wide range of constitutive properties.

4. Summary and conclusions

The TiB_2–Al_2O_3 ceramic composite was successfully produced using reaction synthesis followed by quasi-static consolidation. The microstructure consists of a heterogeneous distribution of titanium diboride (27 vol.%) in an (x-alumina matrix (73 vol.%) with porosity in both phases at grain boundaries as well as within gains. The bulk bodies displayed cracks induced by thermal shock during cooling in air.

The density obtained ranged from 90 to 95.7%. The reported Vickers microhardness values of the composite averaged 23 GPa, which is consistent with the value of 21.6 GPa mentioned in the literature and represents a weighted average between TiB_2 (31.2 GPa) and $A1_2O_3$ (20.0 GPa).

Microscopy (optical, SEM, TEM) revealed a eutectic-like morphology of the TiB_2 phase. The average TiB_2 grain size was found to be 1–2 μm. A third phase was observed along the TiB_2 grain boundaries in both types of specimens. It is believed to be unreacted titanium oxide but would require further investigation to acertain its identification. On the other hand, the (x-alumina phase displayed large dislocation-free grains (20–50 μm). Presence of a liquid phase during reaction and subsequent compaction is confirmed by SEM observation of the TiB_2/Al_2O_3 interface. Micrographs also reveal interface regions of incomplete wetting between the two phases. The overall microstructure displays very few dislocations, which are located within titanium diboride grains.

A simplified thermal analysis of the process was performed in order to obtain an approximation of the temperature evolution as a function of time within the reacted and compressed samples.

The consolidation behavior of TiB_2–Al_2O_3 was studied at strain rates ranging from 10^{-2} to 10^{-1} s^{-1}. Several models for the behavior of hot reacted porous TiB_2–Al_2O_3 have been obtained and compared by using a number of rigid-plastic and power-law creep constitutive models relating yield stress to density and temperature for uniaxial strain compression. This constitutive models yield the temperature dependence of the Al_2O_3–TiB_2 composite. Power-law creep models provide the best fit to the experimental data on axial hot pressing in a rigid die.

In particular, as a first attempt to model the behavior of reacted TiB_2–Al_2O_3 during quasi-static consolidation, good agreement between the Skorohod and McMeeking and Sofronis models and the experimental results is obtained. These models can be adapted to samples of different sizes and different experimental conditions. Extension of such models to other SHS processed materials (TiB_2 and TiC) can be done by considering a more detailed analysis of the variation of temperature with time inside the sample. The variation with temperature of the yield stress of fully dense TiB_2–Al_2O_3 within the experimental range is consistent with values given in the literature for high temperature deformation of both titanium diboride and alumina.

Acknowledgements

We gratefully acknowledge the help provided by W. K. Bluege, W. L.H. Yu, J.C. LaSalvia, and D.A. Hoke. This work has been in part supported by the NSF Division of Manufacturing and Industrial Innovation, Grant DM II–9985472.

References

[1] A.G. Merzhanov, Comb. Flame 13 (1969) 143.
[2] A.G. Merzhanov, I.P. Borovinskaya, Dokl. Akad. Nauk. SSSR (Chem.) 204 (2) (1972) 429.
[3] A.G. Merzhanov, A.K. Filonenko, I.P. Borovinskaya, Dokl. Akad. Nauk SSSR 208 (4) (1973) 122.
[4] A.G. Merzhanov, in: Z.A Munir, J.B. Holt (Eds.), Combustion and Plasma Synthesis of High-Temperature Materials, VCH Publishers, New York, 1990, p. 1.
[5] Z.A. Munir, Am. Ceram. Soc. Bull. 67 (2) (1988) 342.
[6] C.P. Cameron, J.H. Enloe, L.E. Dolhert, R.W. Rice, Ceram. Eng. Sci. Proc. 11 (910) (1990) 1190.
[7] B.H. Rabin, G.E. Korth, R.L. Williamson, J. Am. Ceram. Soc. 73 (7) (1990) 2156.
[8] J.B. Holt, Z.A. Munir, J. Mater. Sci. 21 (1986) 251.
[9] E.A. Olevsky, E.R. Kristofetz, M.A. Meyers, Int. J. Self-Propagating High-Temperature Synthesis 7 (4) (1998) 517.
[10] R.V. Raman, S.V. Rele, S. Poland, J. LaSalvia, M.A. Meyers, A.R. Niiler, J. Metals 3 (1995) 23.
[11] M. Ohyanagi, M. Fukushima, M. Koizumi, Proc. Of the Int. Conf. On Hot Isostatic Pressing, Andover MA, 1996, p. 289.
[12] Y. Myamoto, M. Koizumi, O. Yamada, J. Am. Ceram. Soc. 67 (11) (1984) 224.
[13] Y. Myamoto, Am. Ceram. Soc. Bull. 69 (4) (1990) 686.

[14] O. Yamada, Y. Myamoto, M. Koizumi, J. Am. Ceram. Soc. 70 (9) (1987) 206.
[15] S. Adachi, T. Wada, T. Mihara, Y. Myamoto, M. Koizumi, J. Am. Ceram. Soc. 73 (5) (1990) 1451.
[16] Y. Taneoka, O. Odawara, Y. Kaieda, J. Am. Ceram. Soc. 72 (6) (1989) 1047.
[17] Z.A. Munir, U. Anselmi-Tamburini, Mater. Sci. Rep. 3 (1989) 277.
[18] H.C. Yi, J.J. Moore, J. Mater. Sci. 25 (1990) 1159.
[19] A. Niiler, L.J. Kecskes, T. Kottke, P.H. Netherwood, Jr., R.F. Benck, Technical Report BRL-TR-2951, Ballistic Research Laboratory, Aberdeen Proving Ground, MD, Dec. 1988.
[20] L.J. Kecskes, A. Niiler, J. Am. Ceram. Soc. 72 (4) (1989) 655.
[21] N.N. Thadhani, in: S.C. Schmidt, J.N. Johnson, L.W. Davison (Eds.), Shock Compression of Condensed Matter-1989, Elsevier Science, Amsterdam, 1990, p. 503.
[22] J.C. LaSalvia, L.W. Meyer, M.A. Meyers, J. Am. Ceram. Soc. 75 (3) (1992) 592.
[23] D.A. Hoke, M.A. Meyers, L.W. Meyer, G.T. Gray IIII, Metall. Trans. A 23A (1992) 77.
[24] D.A. Hoke, MS Thesis, University of California, San Diego, 1991.
[25] J.C. LaSalvia, MS Thesis, University of California, San Diego, 1990.
[26] K.V. Logan, J.D. Walton, Ceram. Eng. Sci. Proc. 5 (7-8) (1984) 712.
[27] K.V. Logan, J.T. Sparrow, and W.J.S. McLemore, in *Combustion and Plasno Synthesis of High Temperature Materials*., Z.A. Munir and J.B. Holt Eds., VCH Publishers, New York, 990.
[28] D.J. Johns, Thermal Stress Analysis, Pergamon Press, Oxford, 1965.
[29] R.L. Ashbrook, J. Am. Ceram. Soc. 60 (9–10) (1977) 428.
[30] H.A. Kuhn, C.L. Downey, Int. J. Powd. Metall. 7 (1) (1971) 15.
[31] S.M. Doraivelu, H.L. Gegel, J.S. Gunasekera, J.C. Malas, J.T. Morgan, J.F. Thomas Jr., Int. J. Mech. Sci. 26 (9–10) (1984) 527.
[32] E.A. Olevsky, A. Molinari, Int. J. Plasticity 16 (2000) 1–37.
[33] A.L. Gurson, J. Eng. Mater Technol. 99 (1977) 2.
[34] V.V. Skorohod, Rheological Basis of the Theory of Sintering, Naukova Dumka, Kiev, 1972.
[35] J.R. Ramberg, W.S. Williams, J.Mater. Sci. 22 (1987) 1815.
[36] M.F. Ashby, Background reading, HIP6.0, University of Cambridge, Cambridge, 1990.
[37] P. Sofronis, R.M. McMeeking, Trans. Am. Soc. Met. 59 (1992) 88.